Supporting information

Rational design of nitrogen-doped porous carbon support on single atom catalysts for efficient CO_2 electroreduction

Yejung Choi[a,b,†], Keon-Woo Kim[a,b,†], Byoung Joon Park[c], Tae Yong Kim[c], Yechan Lee[b], Bomi Park[a,b], Jin Kon Kim[a,b,], Jeong Woo Han[c,*]*

[a]National Creative Research Initiative Center for Hybrid Nano Materials by High-level Architectural Design of Block Copolymer

[b]Department of Chemical Engineering, Pohang University of Science and Technology (POSTECH), Pohang, Gyeongbuk 37673, Republic of Korea

[c]Department of Materials Science and Engineering, Research Institute of Advanced Materials, Seoul National University, Seoul 08826, Republic of Korea

[†]These authors contributed equally to this work

[*]Corresponding authors' e-mail: jkkim@postech.ac.kr (J.K.K) and jwhan98@snu.ac.kr (J.W.H)

Experimental section

Chemical reagents

All chemicals were purchased from Sigma-Aldrich, except two PS-*b*-P2VPs (PS(18k)-*b*-P2VP(9k) with a number-average molecular weight (M_n) of PS = 18,000 g mol^{-1}, and M_n of P2VP = 9,000 g mol^{-1}, and the dispersity index ($Đ$) = (1.08); and PS(40k)-*b*-P2VP(9k) with M_n of PS = 40,000 g mol^{-1}, M_n of P2VP = 9,000 g mol^{-1}, and $Đ$ = 1.02), which were purchased from Polymer Source Inc. All the chemicals were used without further purification. Carbon paper (Sigracet 22 BB) was supplied by Fuel Cell Store, Germany. Graphene without mesopores (G) and mesoporous graphitic carbon (mG) with pore sizes of 10 ± 1 nm were purchased from Sigma-Aldrich and used without further purification.

Fabrication of the N-mG support

The N-mG support was prepared via the self-assembly of PS-*b*-P2VP and nickel nitrate hexahydrate ($Ni(NO_3)_2 \cdot 6H_2O$). PS-*b*-P2VP (50 mg) was dissolved in tetrahydrofuran (8 ml), whereas $Ni(NO_3)_2 \cdot 6H_2O$ (100 mg) and citric acid (32 mg) were dissolved in ethanol (2 ml). Citric acid was used to retard the hydrolysis and condensation of $Ni(NO_3)_2 \cdot 6H_2O$. The two resulting solutions were mixed and stirred for 30 min and poured into a petri dish and kept for two days to obtain a mesostructured composite via the evaporation of the solvents. The mesostructured composite was then placed in an oven at 100 °C for one day to completely remove the solvents. Next, the mesostructured composite was catalytically pyrolyzed in a tube furnace using a temperature range of 800–1000 °C for 1 h under a ramping rate of 1 °C min^{-1} and Ar flow (150 sccm). Finally, Ni was removed using 2 M HCl and 2 M HNO_3 under reflux for 48 h to obtain the N-mG supports.

Preparation of NiPc/N-mG, NiPc/G, and NiPc/mG

Single-Ni-atom catalysts were prepared using three supports, namely, N-mG, G, and mG. First, 4 mg of NiPc was added to an ethanol solution (40 ml) containing each support (40 mg). The solution was sonicated for 1 h and subsequently stirred for 24 h at 40 °C. The powders were then obtained after washing three times with ethanol in a centrifuge. The powders were dried and subsequently, thermally treated in a tube furnace at 400 °C for 1 h under Ar flow (150 sccm) to obtain NiPc/N-mG, NiPc/G, and NiPc/mG.

Materials characterization

The thermal behavior of NiPc was analyzed by thermogravimetric analysis (TGA) (SDT Q600, TA instruments, USA). The morphologies of the samples were characterized using a field-emission scanning electron microscope (FE-SEM) (S-4800, Hitachi, Japan) and a high-resolution transmission electron microscope (HR-TEM) (JEM-2200FS, JEOL Ltd., Japan) equipped with an image spherical aberration corrector. High-angle annular dark-field scanning transmission electron microscope (HAADF-STEM) images were acquired using a STEM (ARM 200F, JEOL Ltd., Japan) at the Materials Imaging & Analysis Center in POSTECH, South Korea. The surface areas of the samples were determined via Brunauer–Emmett–Teller (BET) (BELSORP-mini II, Microtrac BEL, Japan) N_2 adsorption measurements. The defect (D) and graphitic (G) characteristics of the supports were examined using a Raman spectrometer (Ram II-Senterra, Bruker). The crystal structures were analyzed via X-ray diffraction (XRD) (D/MAX-2500/PC, Rigaku, Japan), and the chemical states were characterized using an X-ray photoelectron spectroscope (XPS) (Vg Escalab 250, Thermo Fisher Scientific, USA) equipped with a monochromatic Al-Kα radiation source (hν = 1486.9 eV). The nickel content was analyzed by inductively coupled plasma-atomic emission spectroscopy (ICP-AES) (Spectro ARCOS EOP, Spectro, Germany). The Ni K-edge X-ray absorption fine structure (XAFS) data were acquired in the fluorescence mode at the 8C nano-

probe XAFS beamline (BL8C) at Pohang Light Source using the 3.0 GeV storage ring, with a ring current of 250 mA. The X-ray beam was monochromated by a Si(111) double crystal, reducing the beam intensity by 30% to eliminate the higher-order harmonics. The X-ray beam was subsequently delivered to a secondary source aperture through which the beam size was adjusted to 0.5 mm (v) × 1 mm (h). The extended XAFS (EXAFS) k^3-weighted data were obtained over the 1.0–13.0 $Å^{-1}$ range by applying a Hanning window function.

Computational details

The Vienna ab initio simulation package (VASP) and projected augmented wave potentials were used to perform spin-polarized DFT calculations [1, 2]. We considered electronic exchange and correlation by using the revised Perdew-Burke-Ernzerhof functional, employing the generalized gradient approximation [3]. All computations were performed on a plane-wave basis with a cutoff of 500 eV. Using the simulation model, the total energy was calculated using Gaussian smearing with a width of 0.1 eV. The convergence threshold used for the total energy calculations was set between 5–10 eV. Additionally, all geometric optimizations were conducted using the conjugate gradient method that considered all forces acting on each atom and stopped on converging to 0.05 eV/Å for electronic relaxation. The Brillouin zone was sampled using a k-point on a 4 × 4 × 1 Monkhorst-Pack grid [4]. The NiPc structure was modeled by embedding a NiPc molecule (Ni–$C_{32}N_8H_{16}$) onto a graphene supercell (17.32 Å × 17.20 Å, 112 carbon atoms) with periodic boundary conditions. The Ni metal surface was modeled using a 3 × 3 × 3 slab, with the bottom two layers fixed. The vacuum space in the z-direction was adjusted to 20 Å to avoid virtual interactions between the periodic graphene layers. The computational hydrogen electrode model developed by Nørskov et al. was applied to obtain the Gibbs free energy changes (ΔG) of the electrochemical steps involved in the CO_2RR [5, 6]. ΔG was calculated as:

$$\Delta G = \Delta E + \Delta ZPE - T\Delta S - \Delta GU$$

where ΔE is the reaction energy, ΔZPE is the difference in the zero-point energy between the reactants and the products, TΔS is the contribution of the entropic energy at room temperature (T = 298.15 K), and ΔGU = – eU is the effect of the applied electrode potential U on the free energy of the electron transfer steps (e = 1.602 × 10^{-9} C is the elementary charge). The implicit solvent environment was modeled using the VASPsol code, and the relative permittivity was set to 80 [7, 8]. The limiting potential (U_L) of the CO_2RR and HER were obtained using the following equations:

$$U_L(CO_2RR) = -\frac{\max\left(\Delta G_{*COOH},\ \Delta G_{*CO} - \Delta G_{*COOH},\ \Delta G_{CO(g)} - \Delta G_{*CO}\right)}{e}$$

$$U_L(HER) = -\frac{\max\left(\Delta G_{*H},\ \Delta G_{H_2(g)} - \Delta G_{*H}\right)}{e}$$

Electrochemical measurements

The electrochemical measurements were obtained using a PGSTAT302N-type potentiostat/galvanostat in a three-electrode H-type cell separated by a Nafion 117 membrane. The working electrode was prepared as follows. Catalyst ink was prepared by dispersing the catalyst (2 mg) in a mixture containing 720 µl of ethanol and 80 µl of Nafion solution. After sonication for 1 h, the resulting ink (200 µl) was loaded onto carbon paper (1 cm × 1 cm) and dried to obtain a catalyst loading amount of 0.5 mg cm^{-2}. The resulting carbon paper was used as the working electrode, whereas Ag/AgCl and a Pt plate were used as the reference and counter electrodes, respectively. CO_2 was purged with a constant flow rate of 20 sccm to prepare a CO_2-saturated 0.1 M $KHCO_3$ electrolyte for all the measurements. Linear sweep voltammetry (LSV) was conducted with a scan rate of 5 mV s^{-1} in the potential range of 0 to –1.2 V_{RHE}. Chronoamperometry tests were conducted for 1800 s at each potential. Electrochemically active surface area (ECSA) was measured by collecting cycle voltammetry (CV) curves in a potential range of 0.3–0 V_{RHE} with scan rates of 20, 25, 30, 40, and 50 mV s^{-1}. Electrochemical impedance spectroscopy (EIS) was conducted in a frequency range of 100 kHz to 0.1 Hz at the open circuit

potential. The gaseous products obtained during the reaction were monitored via online gas chromatography (GC, Younglin 6500, Korea) equipped with a thermal conductivity detector for H_2 quantification and a flame ionization detector for CO quantification. The liquid products were detected via nuclear magnetic resonance (NMR, Avance III 600, Bruker).

Faradaic efficiency calculation

The Faradaic efficiencies (FEs) of the gaseous products were calculated as follows:

$$FE = \frac{v_{CO_2} \times c \times z \times F}{A \times V_m \times J_{total}} \times 100\ \%$$

where $v_{CO_2}$is the flow rate of CO_2 (20 ml min^{-1}), c is the concentration of the gaseous products detected by online GC (ppm), z is the number of transferred electrons (z = 2 for CO and H_2), F is the Faradaic constant (96485 C mol^{-1}), A is the geometric area of the working electrode (1 cm^{-2}), V_m is the molar volume of gas at 25 °C (24.465 l mol^{-1}), and J_{total} is the total current density (mA cm^{-2}).

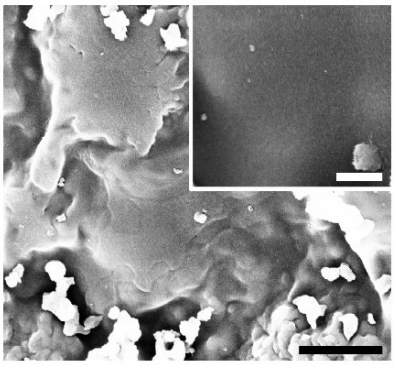

Fig. S1. FE-SEM images after pyrolysis at 900 °C of PS-*b*-P2VP without nickel nitrate (scale bar: 1 μm, inset: 200 nm). Mesostructures are not observed due to the structural collapse caused by the uncontrolled carbonization of PS-*b*-P2VP.

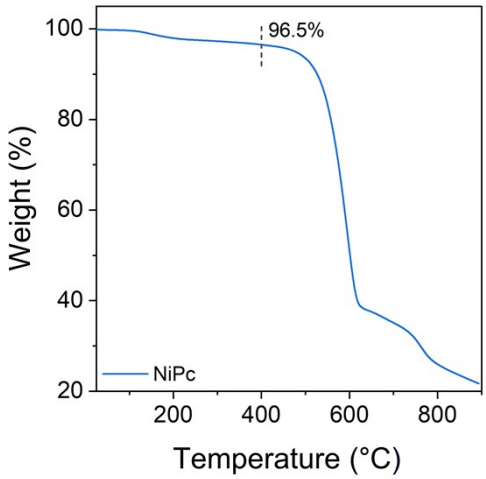

Fig. S2. TGA thermogram of NiPc at a heating rate of 5 °C min^{-1} under an argon atmosphere. At 400 °C, only a slight weight loss of 3.5% was observed due to residual water evaporation.

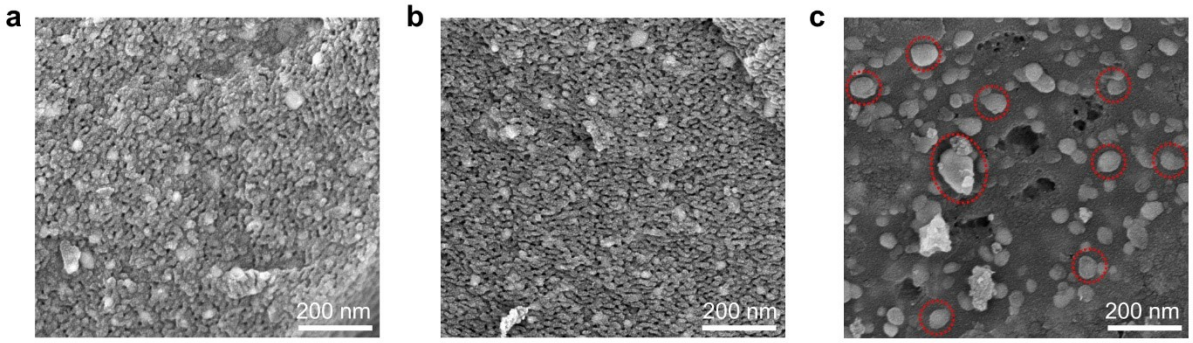

Fig. S3. FE-SEM images of the N-mG supports without Ni etching treatments after catalytic pyrolysis at various temperatures: (a) 800 °C, (b) 900 °C, and (c) 1000 °C. After catalytic pyrolysis at temperatures of 800 °C and 900 °C, a well-established mesoporous structure was obtained; however, at 1000 °C, the thermal expansion of Ni caused structural collapse. The red circle in Fig. S3c indicates the Ni particles agglomerated owing to thermal expansion.

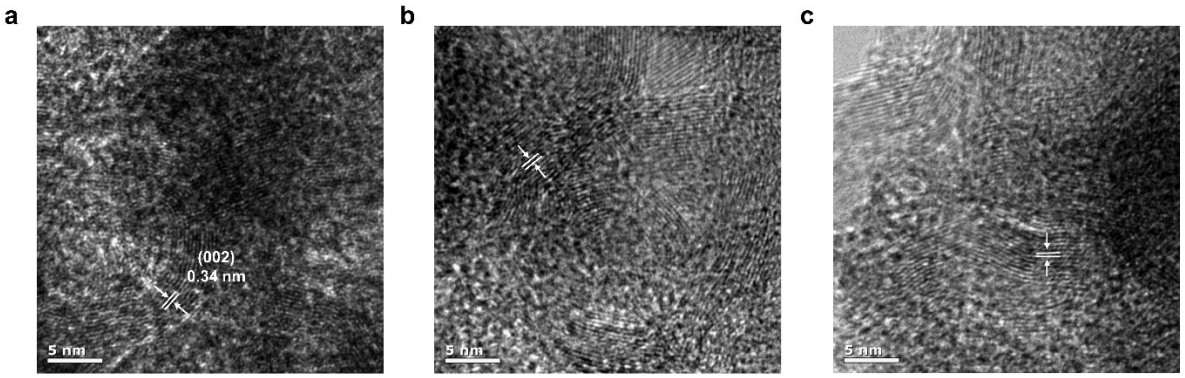

Fig. S4. HR-TEM images of (a) N-mG(800), (b) N-mG(900), and (c) N-mG(1000), showing that all the N-mG supports possess a graphitic carbon layer with a d-spacing of 0.34 nm, which is good agreement with that of graphene sheets.

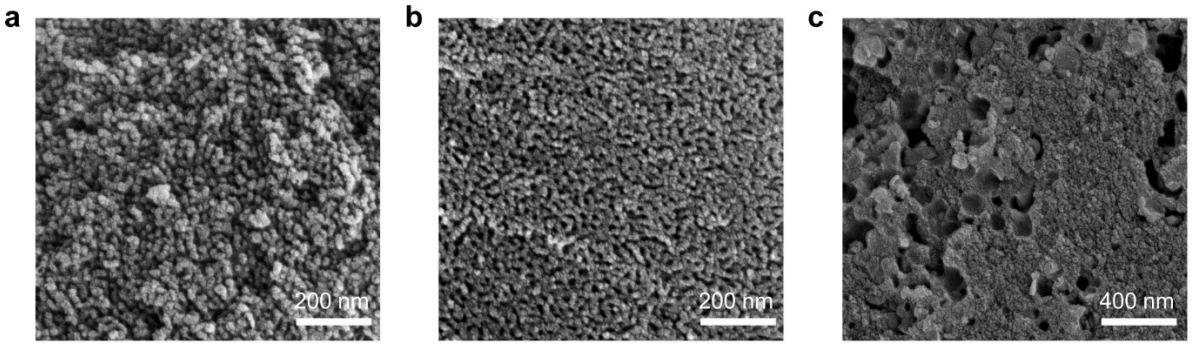

Fig. S5. FE-SEM images of (a) NiPc/N-mG(800), (b) NiPc/N-mG(900), and (c) NiPc/N-mG(1000).

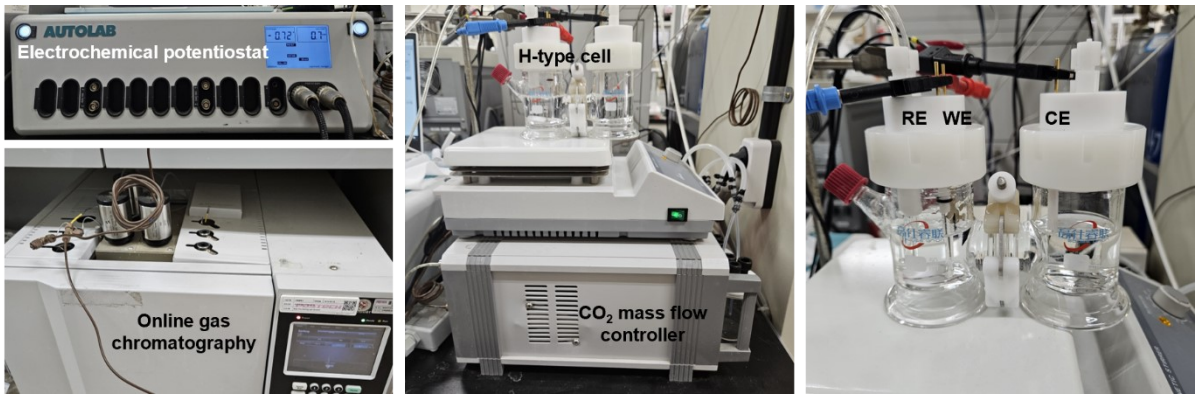

Fig. S6. Photographs of the equipment used for the electrochemical CO_2RR tests.

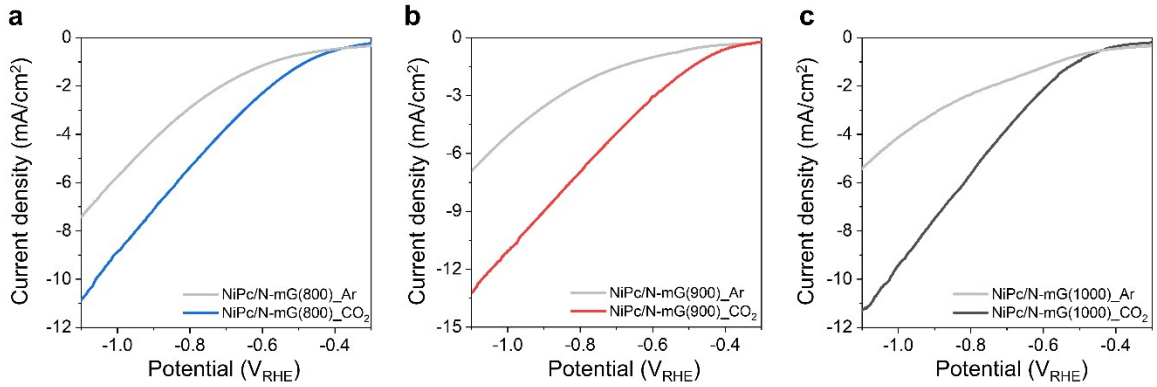

Fig. S7. LSV curves of (a) NiPc/N-mG(800), (b) NiPc/N-mG(900), and (c) NiPc/N-mG(1000) in Ar- and CO_2-saturated 0.1 M $KHCO_3$ electrolytes.

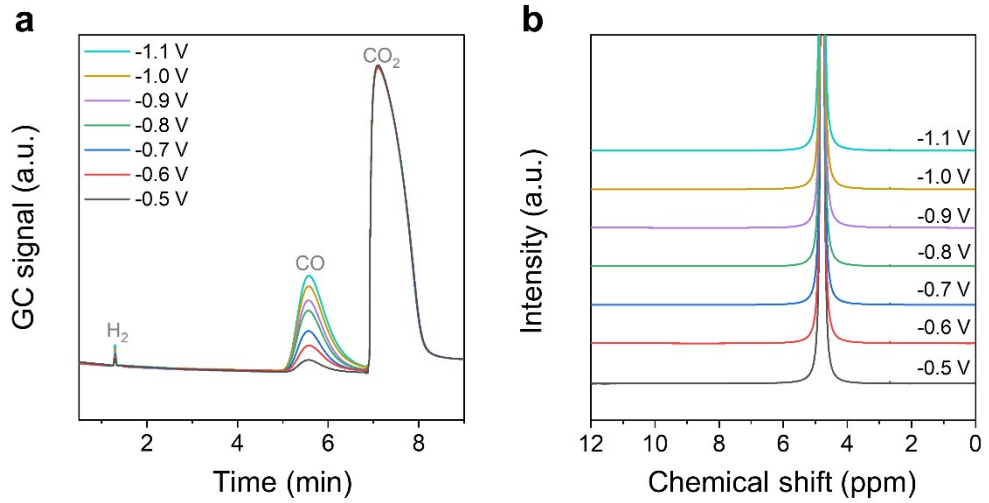

Fig. S8. (a) GC signals for gas products and (b) ^{1}H-NMR spectra of the electrolyte after the CO_2RR electrolysis of NiPc/N-mG(900) for 1800 s at various potentials. The peak at 4.8 ppm in Fig. S8b corresponds to H_2O, which confirms that no liquid product is formed during the CO_2RR.

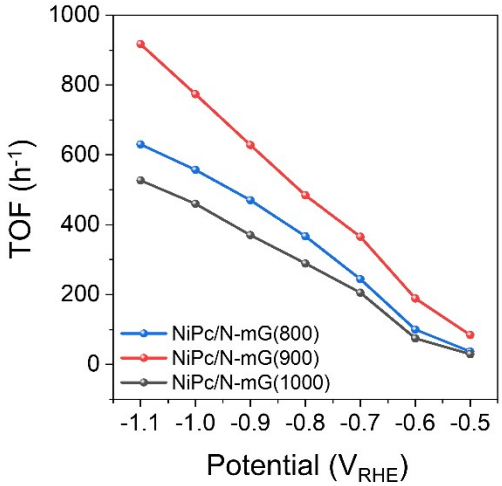

Fig. S9. Turnover frequencies of NiPc/N-mG catalysts.

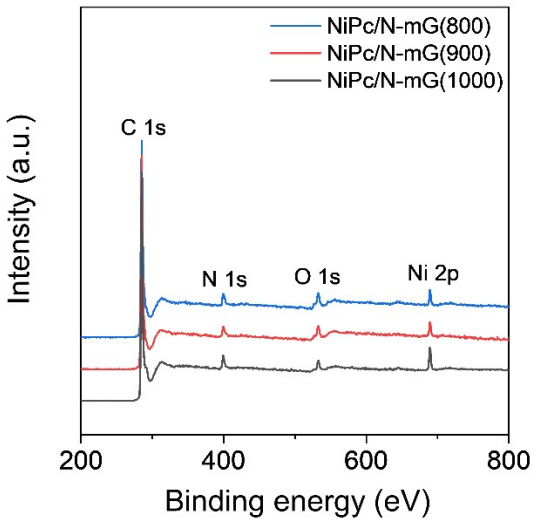

Fig. S10. XPS survey spectra of NiPc/N-mG catalysts. The amount of Ni was 0.65, 0.58, and 0.89 for NiPc/N-mG(800), NiPc/N-mG(900), and NiPc/N-mG(1000), respectively.

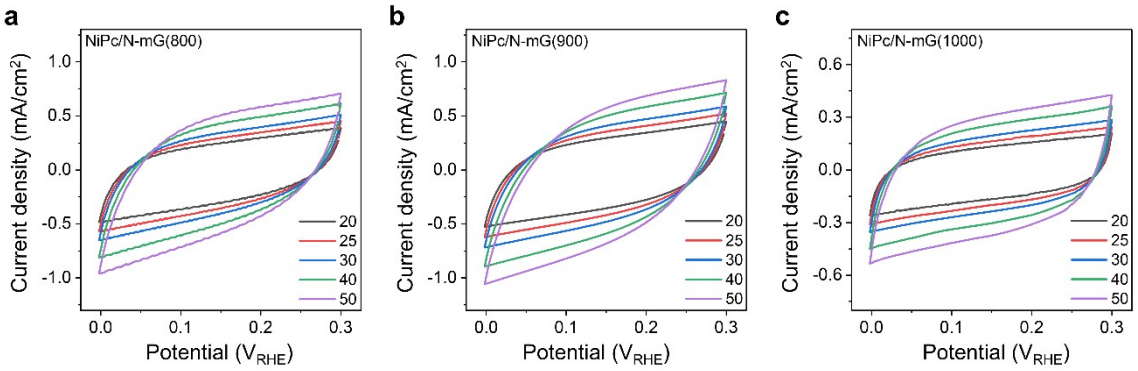

Fig. S11. CV curves of (a) NiPc/N-mG(800), (b) NiPc/N-mG(900), and (c) NiPc/N-mG(1000) at various scan rates (20, 25, 30, 40, and 50 mV s^{-1}).

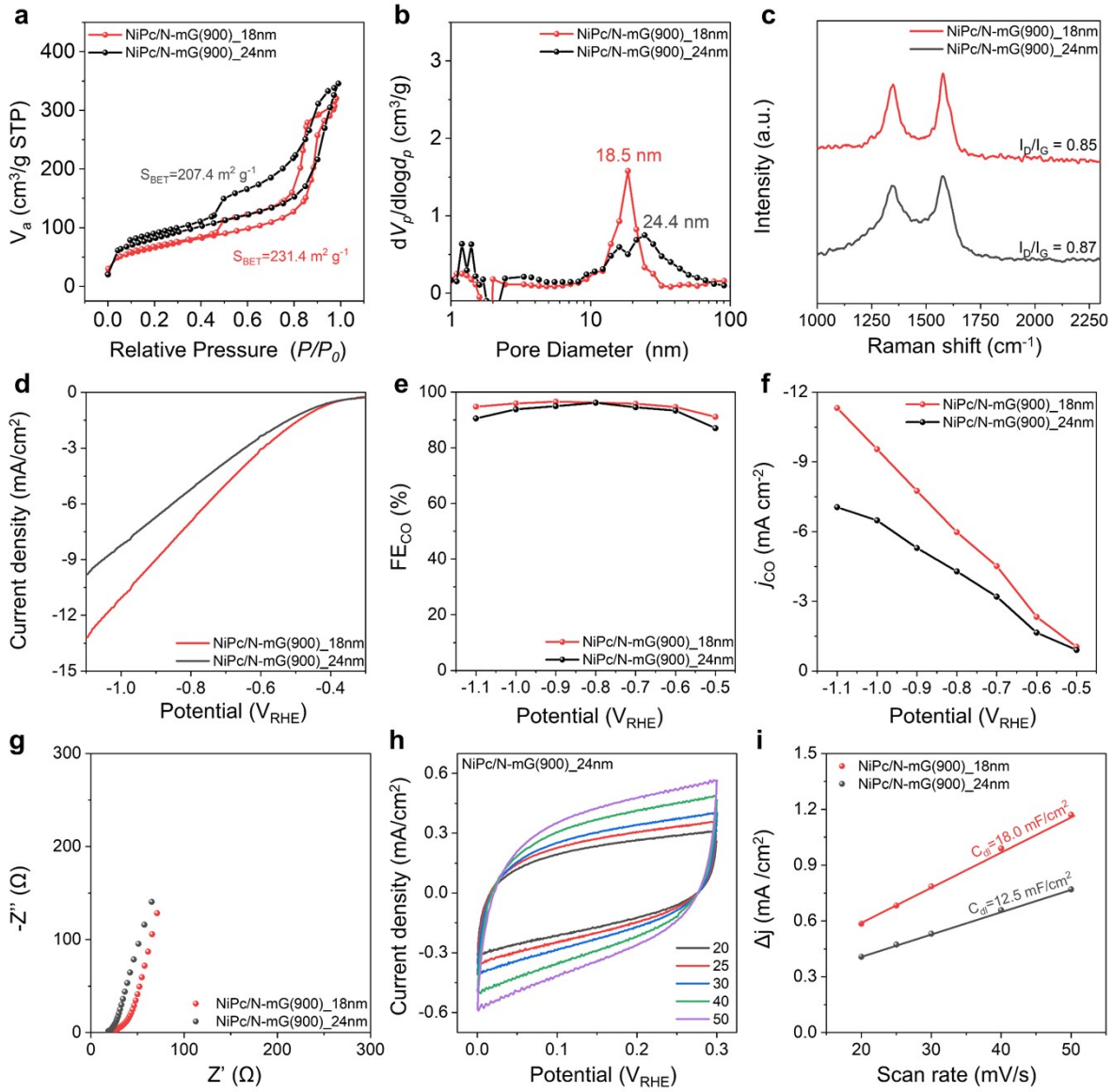

Fig. S12. Comparisons of NiPc/N-mG(900) catalysts with two different pore sizes (18 and 24 nm): (a) Nitrogen adsorption-desorption isotherms, (b) Pore size distributions, (c) Raman spectra, (d) LSV curves, (e) FE_{CO}, and (f) j_{CO}. (g) CV curves of NiPc/N-mG(900)_24nm. (h) Double-layer capacitance, and (i) Nyquist plots.

The porosity of N-mG(900) supports was also controlled by adjusting the volume fraction of PS-*b*-P2VP templates. The PS(40k)-*b*-P2VP(9k) template, with larger PS volume fraction than PS(18k)-*b*-P2VP(9k), resulted in N-mG(900) supports having larger pores of 24 nm (thus, lower surface area), while maintaining a similar degree of graphitization (Fig. S12(a-c)). The NiPc/N-mG(900) with a pore size of 18 nm exhibited higher current density than that with a pore size 24 nm (Fig. S12d). Additionally, it shows slightly higher FE_{CO} across the entire potential range. But, j_{CO} showed greater difference (Fig. S12e,f). The different behavior of j_{CO} and FE_{CO} between two sample is attributed to the different surface area caused by the variation in pore size. Though both catalysts possess pore sizes suitable for effective mass transport, resulting in negligible differences in ion diffusion kinetics (Fig. S12g), N-mG(900) with 18 nm mesopores exhibited larger C_{dl} than that with 24 nm mesopores (Fig. S12h,i), because of larger surface area participating the catalytic reactions.

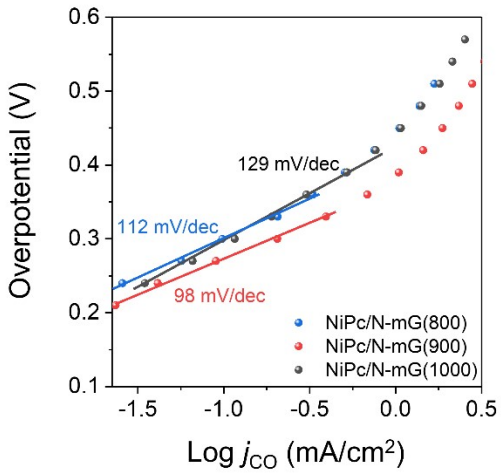

Fig. S13. Tafel plots of the NiPc/N-mG catalysts.

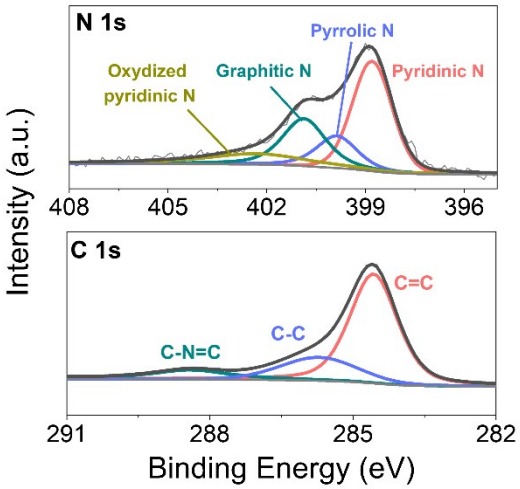

Fig. S14. N 1s and C 1s XPS spectra of NiPc/N-mG(900).

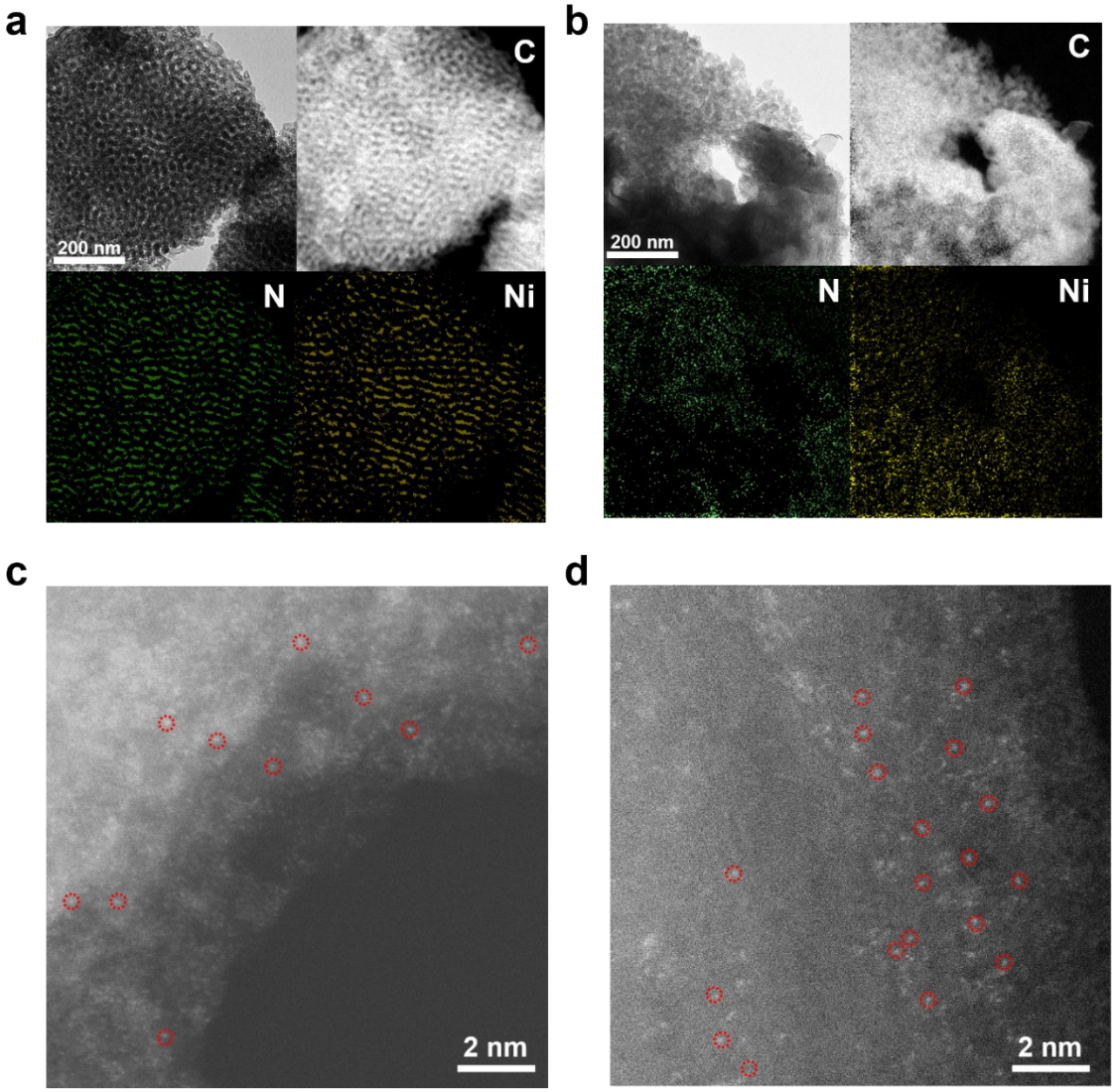

Fig. S15. EELS mappings of (a) NiPc/N-mG(800) and (b) NiPc/N-mG(1000). HAADF-STEM images of (c) NiPc/N-mG(800) and (d) NiPc/N-mG(1000). These results confirmed the uniform distribution of NiPc on the N-mG supports.

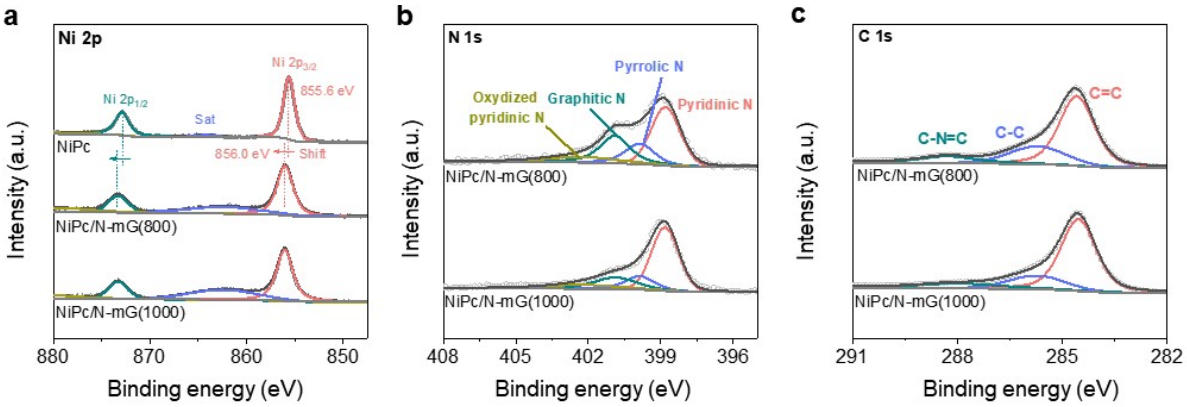

Fig. S16. (a) Ni 2p XPS spectra of NiPc/N-mG(800), NiPc/N-mG(1000), and NiPc. (b) N 1s and (c) C 1s XPS spectra of NiPc/N-mG(800) and NiPc/N-mG(1000).

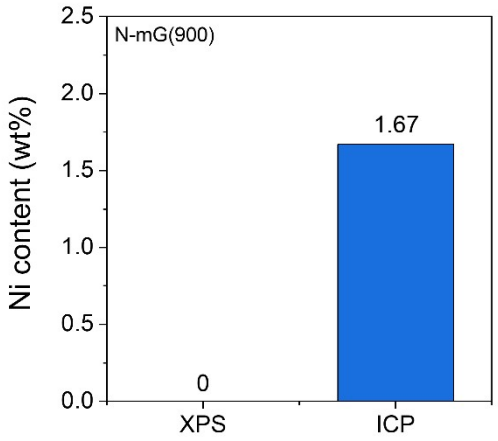

Fig. S17. Ni content in N-mG(900) determined by XPS and ICP-AES measurements. In the ICP-AES analysis, nickel content in N-mG(900) was 1.67 wt%, but it was not detected by XPS. This indicates that the nickel is located within the support framework [9].

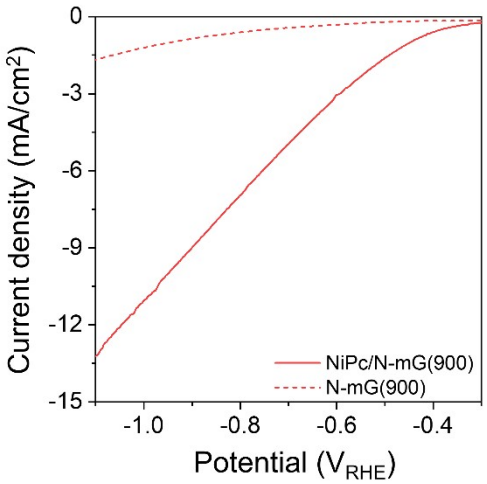

Fig. S18. LSV curves of N-mG(900) support and NiPc/N-mG(900) catalyst in CO_2-saturated 0.1 M $KHCO_3$ electrolyte.

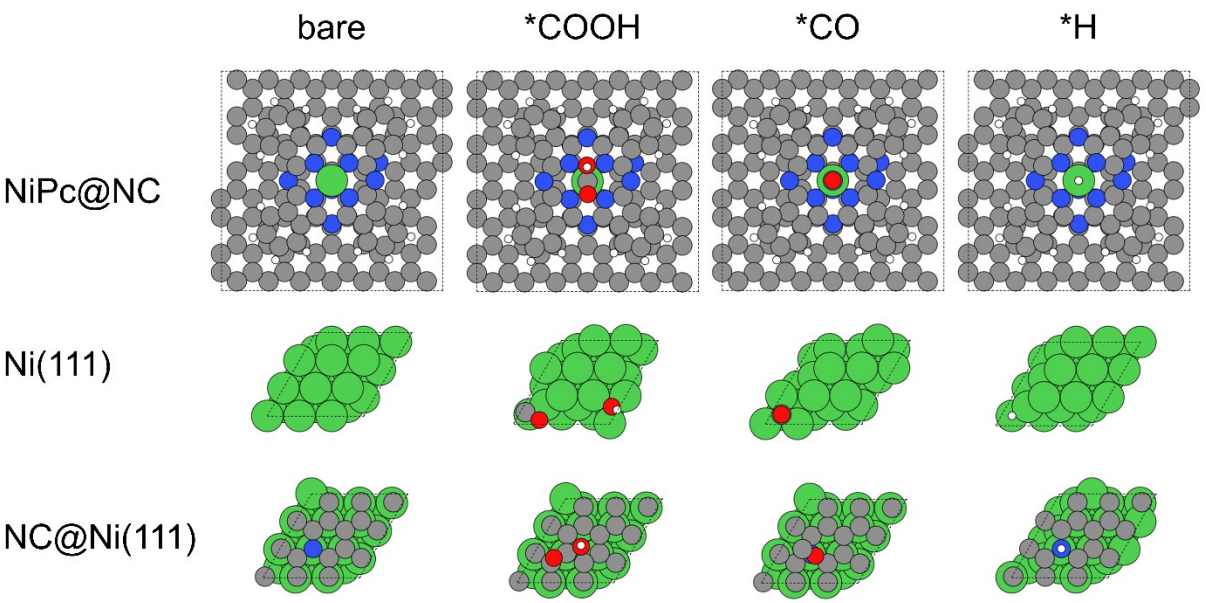

Fig. S19. Atomic structures of the CO_2RR and HER intermediates of NiPc@NC, Ni(111), and NC@Ni(111). The white, gray, red, blue, and green colors represent H, C, O, N, and Ni atoms, respectively.

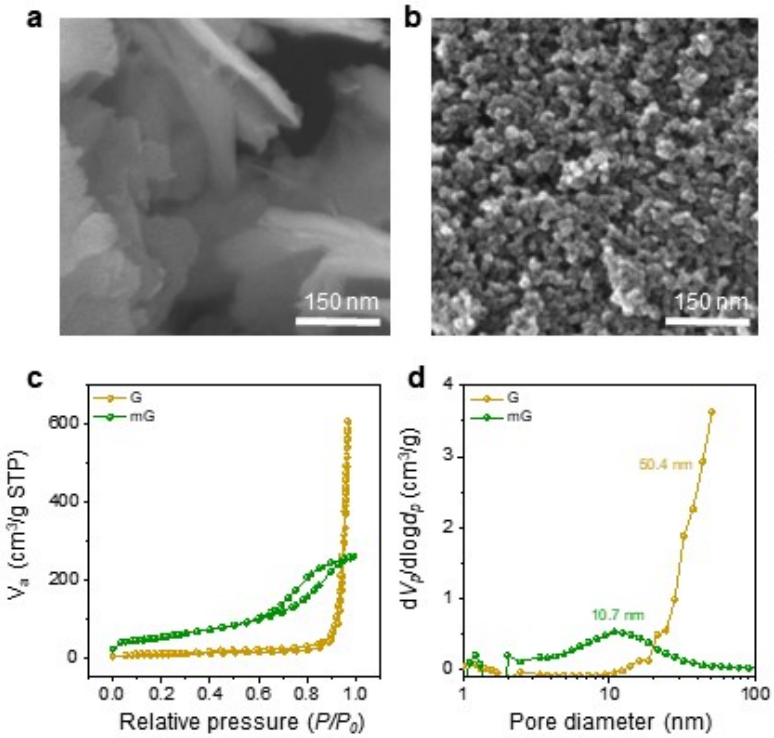

Fig. S20. FE-SEM images of the (a) G and (b) mG supports. (c) Nitrogen adsorption-desorption isotherms and (d) pore size distributions of the G and mG supports. The G and mG supports exhibit sheet-like morphologies and mesoporous structures, respectively. The G support exhibits a type-II isotherm corresponding to a macroporous structure with a predominant pore size of 50.4 nm. The mG support exhibits a type-IV isotherm indicating a mesoporous structure with a predominant pore size of 10.7 nm. The BET surface area of mG (195.1 m^2 g^{-1}) is much larger than that of G (31.3 m^2 g^{-1}), indicating that mesoporous structures are effective at increasing surface area.

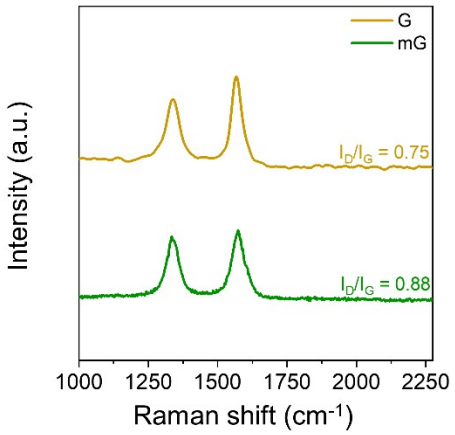

Fig. S21. Raman spectra of the G and mG supports. The I_D/I_G ratios of the G and mG supports are 0.75 and 0.88, respectively. These results show that the mG support has a similar degree of graphitization to that of N-mG(900), whereas the G support has a slightly better graphitization degree.

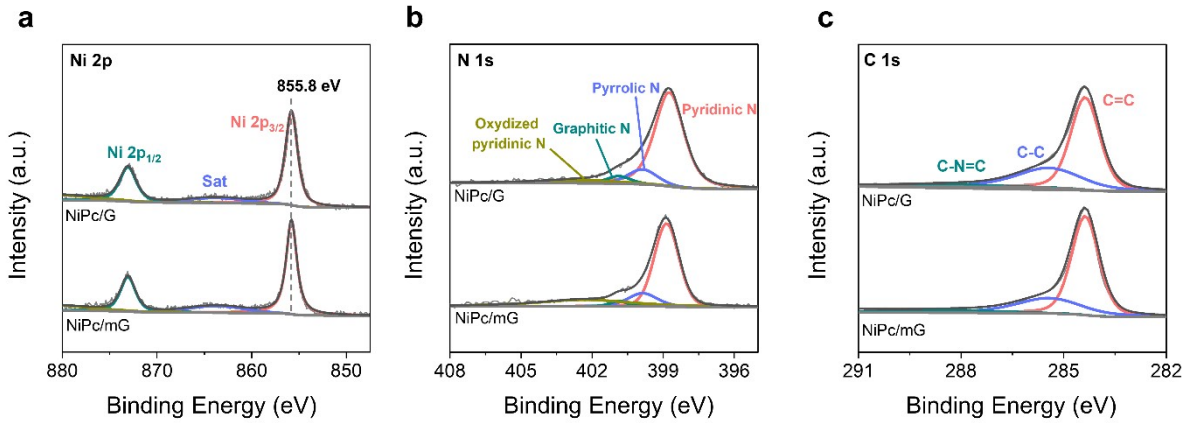

Fig. S22. (a) Ni 2p, (b) N 1s, and (c) C 1s XPS spectra of the NiPc/G and NiPc/mG catalysts. NiPc/G and NiPc/mG exhibit similar chemical compositions, while the characteristic Ni $2p_{3/2}$ peak of Ni^{2+} in NiPc appears at a lower binding energy than that of NiPc/m-G(900) due to the absence of nitrogen in the supports.

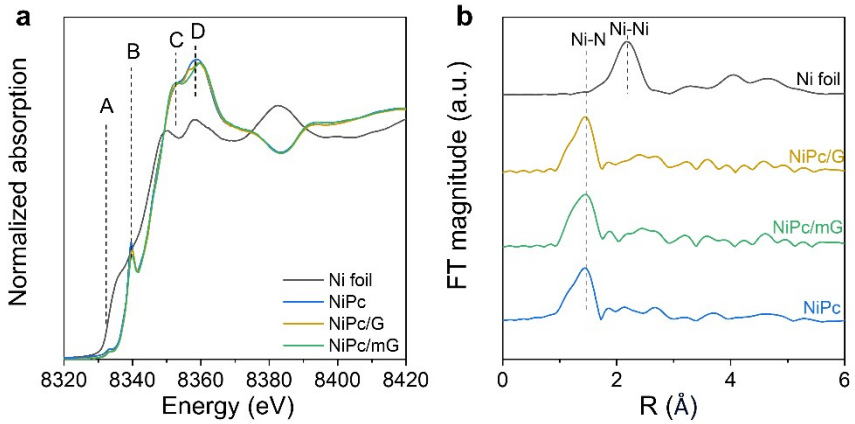

Fig. S23. (a) XANES spectra and (b) k^3-weighted FT-EXAFS spectra of the Ni K-edge of the Ni foil, NiPc/G, NiPc/mG, and NiPc. The XANES spectra of NiPc/G and NiPc/mG exhibit similar peaks (B–D) to those of NiPc. In addition, the FT-EXAFS spectra of NiPc/G and NiPc/mG show only one strong peak at approximately 1.4 Å, corresponding to the Ni–N bond. These results confirm the successful decoration of NiPc on the G and mG supports.

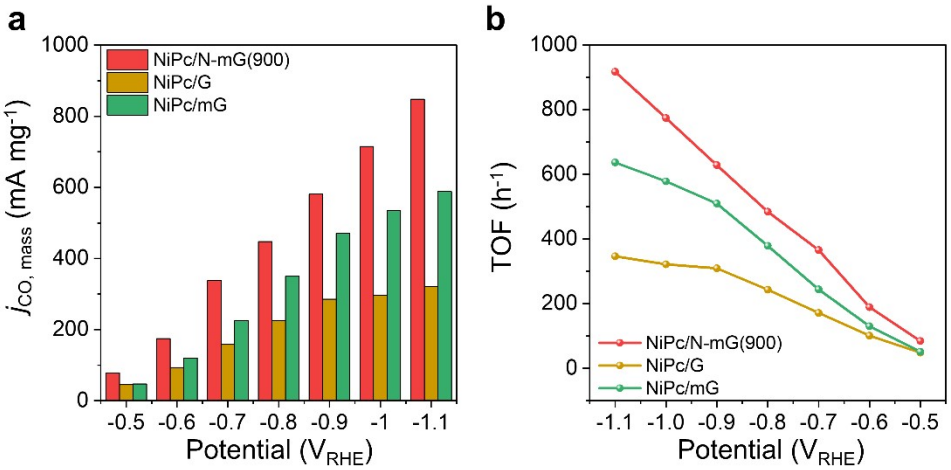

Fig. S24. (a) Mass activities, and (b) turnover frequencies of NiPc/N-mG(900), NiPc/G, and NiPc/mG catalysts.

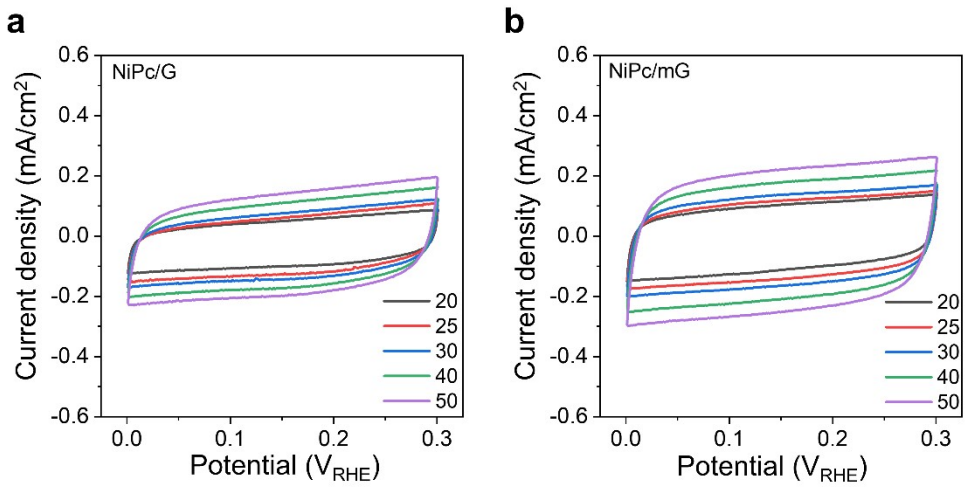

Fig. S25. CV curves of (a) NiPc/G and (b) NiPc/mG at various scan rates (20, 25, 30, 40, and 50 mV s^{-1}).

Table S1. Ni atomic composition in the NiPc/N-mG, NiPc/G, and NiPc/mG catalysts determined via XPS.

Catalysts	Ni atomic composition (at %)
NiPc/N-mG(800)	0.65
NiPc/N-mG(900)	0.58
NiPc/N-mG(1000)	0.89
NiPc/N-mG(900)_24nm	0.51
NiPc/G	0.66
NiPc/mG	0.53

Table S2. Summary of the Ni K-edge EXAFS curve fitting parameters of NiPc/N-mG(900).

Sample	Path	N	R (Å)	σ^2 (Å^2)	R-factor (%)
NiPc/N-mG(900)	Ni-N	4.0	1.875	0.003	1.75
	Ni-Ni	2.7	2.480	0.009	

(N = coordination number, R = interatomic distance, σ^2 = Debye-Waller factor (bond disorder), R-Factor = a measure of the quality of the EXAFS fit.)

Table S3. BET specific surface areas and pore volumes of all the supports.

Supports	BET specific surface area (m^2 g^{-1})	Pore volume (cm^3 g^{-1})
N-mG(800)	246.8	0.6138
N-mG(900)	231.4	0.4953
N-mG(1000)	419.5	4.4787
N-mG(900)_24nm	207.4	0.5908
G	31.3	0.9397
mG	195.1	0.4034

Table S4. Comparison of catalytic performance for the electroreduction of CO_2 to CO on Ni based single atom catalysts.

Catalysts	Active site	Con. Of $KHCO_3$ (M)	FE_{CO} (%)	J_{CO} (mA cm^{-2})	Potential (V_{RHE})	Partial window over 90% FEco (V_{RHE})	References
NiPc/N-mG(900)	**Ni-N_4**	**0.1**	**96.4** **94.8**	**7.8** **11.3**	**–0.9** **–1.1**	**–0.5 ~ –1.1**	**This work**
NiSA-NGA-900	Ni-N_4	0.5	90.2	6.4	–0.8	–0.8	10
Ni/HMCS-3-800	Ni-N_4	0.5	~95	10.5	–1.0	–0.7 ~ –1.1	11
Ni-N-ANBC	–	0.1	97	~2.7	–0.93	–0.82 ~ –1.15	12
Ni SAs-NCW	Ni-N_4	0.1	92.1	11.4	–0.46	–0.46	13
Ni_1-N-C-50	Ni-N_4	0.5	96	~7	–0.7	–0.65 ~ –0.95	14
Ni-NCN	Ni-N_4	0.5	97	9.8	–0.83	–0.63 ~ –1.13	15
Ni_1-N-C	Ni-N_4	0.5	~95	~2	–0.7	–0.60 ~ –0.95	16
Ni-N-CNTs-10	Ni-N_4	0.5	98.3	5.3	–0.65	–0.60 ~ –0.75	17
Ni SAC	Ni-N_4	0.5	85	12	–0.8	–	18

References

1. G. Kresse and J. Furthmüller, *Phys. Rev. B*, 1996, **54**, 11169.
2. G. Kresse and J. Hafner, *Phys. Rev. B*, 1993, **47**, 558.
3. B. Hammer, L. B. Hansen and J. K. Nørskov, *Phys. Rev. B*, 1999, **59**, 7413.
4. H. J. Monkhorst and J. D. Pack, *Phys. Rev. B*, 1976, **13**, 5188.
5. J. K. Nørskov, J. Rossmeisl, A. Logadottir, L. Lindqvist, J. R. Kitchin, T. Bligaard and H. Jonsson, *J. Phys. Chem. B*, 2004, **108**, 17886-17892.
6. J. Rossmeisl, Z.-W. Qu, H. Zhu, G.-J. Kroes and J. K. Nørskov, *J. Electroanal. Chem.*, 2007, **607**, 83-89.
7. K. Mathew, V. Kolluru, S. Mula, S. N. Steinmann and R. G. Hennig, *J. Chem. Phys.*, 2019, **151**.
8. K. Mathew, R. Sundararaman, K. Letchworth-Weaver, T. Arias and R. G. Hennig, *J. Chem. Phys.*, 2014, **140**.
9. S. Liang, Q. Jiang, Q. Wang and Y. Liu, *Adv. Energy Mater.*, 2021, **11**, 2101477.
10. K. Mou, Z. Chen, X. Zhang, M. Jiao, X. Zhang, X. Ge, W. Zhang and L. Liu, *Small*, 2019, **15**, 1903668.
11. W. Xiong, H. Li, H. Wang, J. Yi, H. You, S. Zhang, Y. Hou, M. Cao, T. Zhang and R. Cao, *Small*, 2020, **16**, 2003943.
12. S. Fu, B. Izelaar, M. Li, Q. An, M. Li, W. de Jong and R. Kortlever, *Nano Energy*, 2024, 110461.
13. H. Chang, H. Pan, F. Wang, Z. Zhang, Y. Kang and S. Min, *Nanoscale*, 2022, **14**, 10003-10008.
14. M. Wen, N. Sun, L. Jiao, S. Q. Zang and H. L. Jiang, *Angew. Chem.*, 2024, **136**, e202318338.
15. C. Lv, K. Huang, Y. Fan, J. Xu, C. Lian, H. Jiang, Y. Zhang, C. Ma, W. Qiao and J. Wang, *Nano Energy*, 2023, **111**, 108384.

16. L. Jiao, J. Zhu, Y. Zhang, W. Yang, S. Zhou, A. Li, C. Xie, X. Zheng, W. Zhou and S.-H. Yu, *J. Am. Chem. Soc.*, 2021, **143**, 19417-19424.

17. S. Wu, F. Yi, D. Ping, S. Huang, Y. Zhang, L. Han, S. Wang, H. Wang, X. Yang and D. Guo, *Carbon*, 2022, **196**, 1-9.

18. Q. Pan, Y. Chen, H. Li, G. Ma, S. Jiang, X. Cui, L. Zhang, Y. Bao and T. Ma, *J. Mater. Chem. A*, 2024, **12**, 20035-20044.